Large rotations of the grain-scale stress tensor during yielding set the stage for failure

Jishnu J. Bhattacharyya[1*], Darren C. Pagan[2], Sean R. Agnew[1]

[1]University of Virginia, Charlottesville, VA, 22904.

[2]Cornell High Energy Synchrotron Source, Cornell University, Ithaca, NY 14853.

*Correspondence to: jjb4cp@virginia.edu

Abstract

The stress-state within individual grains in a polycrystal determine the fate of the aggregate including mechanical failure. By tracking the evolution of the stress tensor throughout the elastoplastic transition, large rotations of the stress state, which have long been theorized to occur, are observed experimentally for the first time. These stress rotations (~15°) are more than an order of magnitude larger than the concomitant crystallographic lattice reorientations (~0.9°) well-known to occur during metal plasticity. Furthermore, these rotations are accompanied by a decrease in stress triaxiality within certain grains, promote strain softening, and set the stage for failure at an early stage of deformation. These results provide a completely new perspective through which to contemplate the question of "hot-spots" responsible for failure of high-performance structural materials.

Keywords: titanium, stress rotation, synchrotron diffraction, failure, stress-state

1. Introduction

Highly engineered polycrystalline, metallic alloys are an integral part of the modern society and are at the heart of infrastructure, manufacturing, energy production, and transportation sectors. Sustainable performance relies on the ability of these materials to withstand design loads and resist failure. Scientists and engineers have increasingly employed a physics-based, multiscale modeling approaches to obtain a detailed description and understanding of polycrystalline deformation behavior. This strategy necessitates well-designed experiments for model validation (Sangid, 2020). At low homologous temperatures, under high stresses, the motion of dislocations is the primary mechanism for plastic deformation in most crystalline materials. Thus, quantifying the stress-state within the individual grains of a polycrystalline material is key for understanding plastic deformation. Furthermore, these stresses play a critical role in determining damage via initiation of shear bands, cracks and voids, in a loaded polycrystal. Notably, the accumulation of damage due to localized plasticity during cyclic loading leads to fatigue, which is one of the main failure mechanisms in structural components (e.g. Gagg and Lewis, 2009). The elastoplastic transition (also known as yielding) is particularly relevant, since fatigue can occur at stresses well below the macroscopic yield strength, where only a fraction of grains may undergo dislocation motion during cyclic loading. Due to the inherent elastic and plastic anisotropy of single crystals, the stress (and strain) levels within the individual grains of a polycrystal can strongly vary, e.g. stiffer grains share a larger stress. As a result, significant grain-scale heterogeneity develops where, e.g., a distinct dislocation substructure evolution may occur in grains of different orientations (Jakobsen et al., 2006, 2007).

A Single Crystal Yield (hyper) Surface (SCYS) is a map in six-dimensional stress space, which delineates the elastic conditions from those which give rise to plasticity. A slip system induces a (hyper) facet of the SCYS in stress space, and the direction of plastic straining on that system is perpendicular to that facet. Facets from all slip systems of highly symmetric crystals form a closed surface, the inner envelope of which is the SCYS. For the rate independent case, slip occurs if the resolved shear stress (RSS) on a slip system is equal to the critical resolved shear stress (CRSS), on that system. For the rate dependent case, the CRSS is a function of temperature and strain-rate and the strain rate sensitivity of the material is an important parameter that determines the "roundness" of the single crystal yield potential (SCYP). The seminal theoretical works of Kocks (Kocks, 1970; Kocks et al., 1983) followed by finite element-based full-field polycrystal plasticity simulations of Dawson's research group (e.g., Ritz et al., 2010) highlighted the fact that the crystal stress-state may strongly reorient during the elastoplastic transition. These rotations are posited to occur along 'facets' and 'edges' of the SCYS towards stress 'vertices' where multiple slip systems are simultaneously activated, in order to accommodate arbitrary straining directions and maintain compatibility among the grains. Since then, several other finite element-based simulation studies have also shown that the crystal stress state tends to align with a vertex of the SCYS (Han et al., 2012, 2013; Han and Chung, 2012). However, the experimental evidence for such predictions have been lacking.

Figure 1 shows a schematic two-dimensional SCYS defined by three slip systems (one per pair of parallel facets). A portion of the SCYS is magnified to illustrate the concept of stress rotation. For simplicity, isotropic elasticity and perfect plasticity are assumed, since extension to the completely general case (e.g. Lee et al., 2017, 2018) does not alter the concept. Prior to yielding (at 1), the material is elastic, and as soon as the material yields (at 2) the total straining

direction is now (within an infinitesimal strain framework) the algebraic sum of two components; the plastic strain increment, which is normal to the facet of the yield surface, and the elastic strain increment. With deformation, the stress and strain tensor evolve in a manner such that stress equilibrium, strain compatibility, and the grain's boundary conditions are satisfied simultaneously. Due to interactions with neighboring grains, the total straining direction of a grain may change with deformation and, consequently, the stress will rotate in order to produce the correct total strain increment and maintain compatibility among the grains (e.g., at 3). If the stress state rotates to a vertex where multiple slip systems intersect, then a range of plastic straining directions can be accommodated by a linear combination of the involved slip systems, (at 4). This implies that the crystal stress-state will tend toward the vertices (or at least edges) of the SCYS, rather than only rotating toward the macroscopic applied stress (Kocks, 1970; Kocks et al., 1983; Ritz et al., 2010).

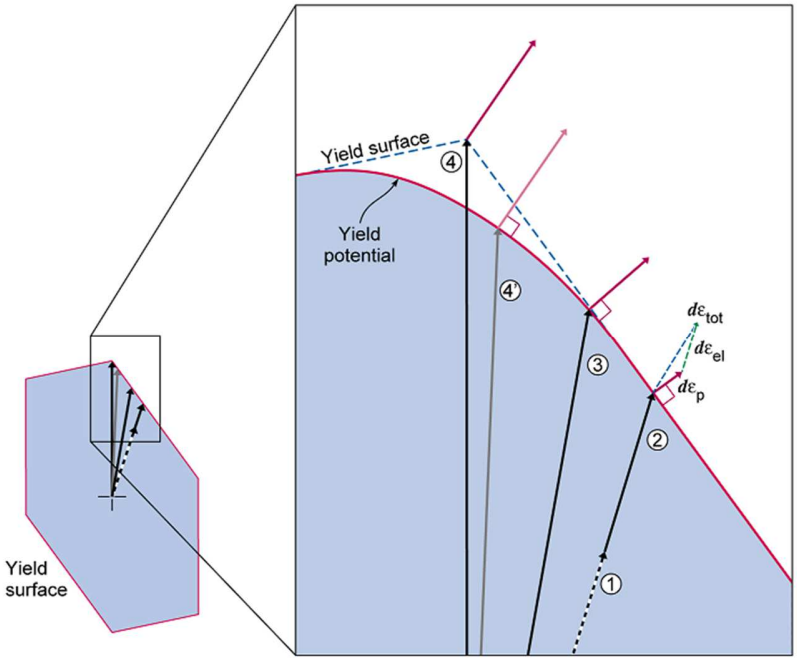

Figure 1. Schematic of the single crystal yield surface (SCYS)**,** with a magnified view, describing the relation between the direction of stress (black arrows) and the direction of plastic strain increment, $d\varepsilon_p$(red arrows) at different stages of elastoplastic transition. The total strain increment, $d\varepsilon_{tot}$ is comprised of an elastic, $d\varepsilon_{el}$ and a plastic component. The stress rotates towards a vertex to produce the required strain increment. For the rate dependent single crystal yield potential (SCYP), the same straining direction is achieved before the stress reaches the vertex.

The specific vertex towards which the grain stress-state rotates will depend on both the boundary conditions imposed on a specific grain and its crystallographic orientation. Kocks (1970) emphasized that, in order to maintain compatibility among the grains in a polycrystal, the resulting conditions of "polyslip" are the norm beyond the elastoplastic transition.

An important point to note is that as the stress-state rotates, the magnitudes of the stresses may also change. Thus, the rotation of the stress tensor is potentially accompanied by an alteration of the nature of the stress state, e.g. the stress triaxiality, which is known to have a significant effect on failure of materials (Lou et al., 2014; Papasidero et al., 2015).

2. Material and methods

2.1 Sample and ex-situ characterization

A metastable β-Ti alloy, Timetal-18 with composition, 5.5Al-5V-5Mo-2.4Cr-0.75Fe-0.15O (in wt.%) (Fanning, 2011; Lebrun et al., 2014), was used for this study because a relatively low modulus and high yield strength provide the best combination for minimizing the experimental uncertainty in the diffraction-based assessments of lattice strain (and therefore stress). Rectangular sections were machined out from the as-received rolled plate with bimodal microstructure, which was then subjected to β solution heat treatment, under Ar atmosphere, at 910°C for 1h, followed by water quenching (SHTQ). The resulting microstructure is large grained (~200 μm), essentially single phase with a BCC crystal structure as determined from selected area electron diffraction (SAED) within a TEM. Substructure with intragranular

misorientations of <0.7° were present. Further details about the microstructure and the grain size distribution are presented elsewhere (Bhattacharyya et al., 2020, 2021). Tensile specimens with loading axis parallel to the rolling direction (RD) of the plate were electro-discharge machined from the heat treated sections and were used for the in-situ diffraction experiment.

2.2 High-energy X-ray diffraction microscopy (HEDM)

The in-situ diffraction experiment was conducted at F2 station at Cornell High Energy Synchrotron Source (CHESS). A monochromatic source radiation of 61.332 keV was used. A tensile specimen with 1.0 x 1.0 mm^2 gage cross-section was deformed under uniaxial tension up to ~6% strain (failure), using the Rotation and Axial Motion System (RAMS2) load frame (Blank et al., 2016; Shade et al., 2015). Data up to a total strain of 2.5% is used in the present study. A crosshead displacement rate of ~10 nm/s was imposed which corresponds to a strain rate of $\sim 1 \times 10^{-6}$ s^{-1}.

The relationship between the sample and the laboratory coordinate system is such that the beam direction is along $-\mathbf{z} \parallel$ TD and the loading axis is along $\mathbf{y} \parallel$ RD, prior to sample rotation. An optical camera placed at the side collected images of the sample surface (**x** plane) that were processed using a custom digital image correlation (DIC) script to calculate macroscopic strains. Output from a load cell was used to calculate the macroscopic stress on the sample.

Diffraction patterns (Debye rings) were collected continuously and recorded on two Dexela 2923 detectors located at a distance of 735 mm behind the sample, as the sample deformed and rotated 360° about the tensile loading axis, **y**, at 0.25° increments, with exposure times of 0.25 s, resulting in a total of 1440 diffraction images per scan. Each scan took about 6 min, which includes the time for the detectors to output the data. Prior to the in-situ experiment, calibration data (sample to detector distance, detector tilts, and detector distortions) were

obtained using a CeO_2 powder standard and finely calibrated (including tilt of the rotation axis) using a ruby crystal standard.

The diffraction peaks were indexed with respect to their (hkl) and grains of origin, due to a judicious balance between the size of the diffracting volume and the grain size. Details of the far-field (ff-HEDM) data reduction and calibration have been published elsewhere (Bernier et al., 2011; Edmiston et al., 2011, 2012) and the data reduction procedure for this experiment involved first identifying the ff-HEDM peak locations ($2\theta, \eta$ & ω) in order to determine the center-of-mass, crystallographic orientation and elastic strain tensor of individual grains in the diffracted volume by the HEXRD package (https://github.com/joelvbernier/hexrd).

The quality of the indexing of a diffraction pattern is determined by two parameters: the *completeness* and the goodness-of-fit (χ^2) value. Depending on the choice of threshold values of these two parameters, a trade-off is being made between confidence in the grain quantities themselves and the statistical relevance of the number grains being analyzed. As the completeness and χ^2 metrics become more stringent, the number of grains analyzed decreases, but the confidence in the conclusions drawn from this subset of grains increases. Here, metrics are chosen heuristically to strike a balance between these competing considerations.

Details regarding the completeness and the χ^2 metrics are given elsewhere (Bhattacharyya et al., 2021). In brief, the "completeness" is defined as the ratio between the number of predicted diffraction peaks (typically ~100) to that observed experimentally. A threshold value of 90% (or 0.9) is used throughout, at each step. The χ^2 value is computed in the normal way, based upon the residual between the measured and predicted diffraction events. A χ^2 minimization algorithm is employed which iteratively varies the components of orientation, position, and strain of the grain to obtain a best fit. A χ^2 value of less than 0.05 was deemed a

good fit and was employed in the present work. During plastic deformation, the multiplication of dislocations distorts the diffraction peaks and thus degrades the quality (peaks spreading as well as splitting up along η & ω), which inhibits successful indexation. Thus, the completeness and the χ^2 value degrade with straining. The elastic strain values are particularly sensitive to the quality of the diffraction peaks, hence to these metrics.

The near-field experiment was conducted on the undeformed sample to characterize the 3D microstructure. A LuAg:Ce scintillator coupled with a 5X objective lens to a Retiga 4000DC CCD camera was used to record the raw data. The detector system has 2048 pixels by 2048 pixels with an effective pixel size of 1.48 μm. The scintillator was placed 6.50 mm from the sample. For these measurements, a 2.5 mm (width) × 0.15 mm (height) beam cross section was used and 6 adjoining vertical scans were carried out to characterize the central 900 mm height of sample (the same region which was characterized by the ff-HEDM experiment described above.) For each of these 6 layers, diffraction patterns were collected at every 0.25° as the sample was rotated 360° in ω resulting in a total of 1440 diffraction images.

Initially, 105 grains were identified by ff-HEDM of which 101 were successfully reconstructed by the nf-HEDM technique, whereas only 31 grains satisfied the completeness and the χ^2 at 0.025 strain. As a reminder, only data obtained from those grains for which the *completeness* is high (> 90 %) and the χ^2 value is low (< 0.05) are used at a given strain level.

In order to classify the grains based on their strain hardening behavior, a total of 65 grains were considered, each of which satisfy the completeness and χ^2 threshold criteria up to at least 1.5% strain. Out of these, 23% of the grains show a flat response (neither hardening or softening), 37% of the grains exhibit hardening, 32% of the grains show a softening response, and 8% of the grains exhibit erratic behavior.

2.3 Micro-computed tomography (μCT)

Following the far-field scans, transmission radiographs were collected as the sample was rotated 360° about the tensile loading axis, **y**, at 0.1° rotation increments, using a Retiga 4000DC camera coupled to a LuAG:Ce scintillator with a 5× lens (1.48 μm effective pixel pitch) placed 6 mm from the sample. 3-D tomographic reconstructions were generated from the raw radiographs using custom Python scripts based on TomoPy, an open-source Python package (Gürsoy et al., 2014). The spatial resolution of the μCT reconstructions are ~ 1.45 μm.

2.4 Lattice rotation

The lattice rotation of the grains is quantified as the evolution of the misorientation, with respect to their initial orientation, and is computed according to: $r_{j0} = \frac{R_j - R_0 + (R_0 \times R_j)}{1 + R_0 \cdot R_j}$, where, r_{j0} is the misorientation between the orientation at the j^{th} step, R_j, and the initial one, R_0, all represented as Rodrigues vectors (Becker and Panchanadeeswaran, 1989). The angle by which the crystal rotates with reference to the initial position, is given by $\theta_{j0} = 2\tan^{-1}\|r_{j0}\|$.

2.5 Rotation of the grain stress tensor

The diffraction experiment described above provides the complete grain-level elastic strain tensor, the grain position (centroid), and the crystallographic orientation of individual grains embedded within the polycrystalline specimen. The stress tensor for a given grain is calculated from the elastic strain tensor, the crystallographic orientation, and the single crystal stiffness coefficients, using Hooke's law and single-crystal elastic constants determined previously (Bhattacharyya et al., 2020). In this work, the eigenvalues (principal stress components) and the eigenvectors (directions of the principle components) of the stress tensor are used. While the stress rotation is characterized by the changes of the orientation of the

eigenvectors, the stress-state e.g. triaxiality is determined in the normal way as the mean stress divided by the von Mises equivalent (i.e. by the eigenvalues). Obviously, a pure rotation without any changes in the three principal stresses would leave the triaxiality unchanged.

The angle between the eigenvector of the maximum principal stress, v_{max}, and the uniaxial macroscopic loading condition, Y = [0,1,0], i.e. $\theta = \cos^{-1}(v_{max} \cdot Y)$ is a measure of 'coaxiality'. Note, in prior works, researchers have defined coaxiality as $\theta = \cos^{-1}\left(\frac{\sigma_{axial} \cdot \sigma}{|\sigma_{axial}||\sigma|}\right)$, where the macroscopic applied stress $\sigma_{axial} = [0, \sigma_{yy}, 0,0,0,0]$ and σ is the grain stress, and they have also observed that the stress coaxiality increases with straining (Lienert et al., 2009; Chatterjee et al., 2016; Juul et al., 2017; Turner et al., 2017). It is important to keep in mind that neither of these definitions of coaxiality completely characterizes the rotation, since it describes only one of the angles viz. the one corresponding to the eigenvector of the maximum principal stress and the macroscopic stress along the loading direction.

To completely quantify the rotation of the stress-state, the misorientation (e.g. axis-angle pair) between the stress-state and a reference is required. Since the rotation which occurs *during* yielding is of interest, a strain level of 0.008 which coincides with the onset of yielding (the proportional limit) is chosen as the reference, and the misorientation between the eigenvectors of the stress tensor of each grain are computed with respect to the eigenvectors of the stresses corresponding to this reference strain.

2.6 Coaxiality with stress vertex

In order to examine whether the grain-level stresses headed toward a vertex, the following strategy was adopted. First, all 56 vertices of the SCYS corresponding to 5 or more independent <111>{110} slip systems were examined, and the coaxiality of the stress with all these vertices were computed. The vertex which yielded the minimum coaxiality *at the end* of

the elastoplastic transition (applied strain 0.015) was chosen, and then the coaxiality between this vertex and the stresses at different strain levels was computed. Examples from representative grains show either a monotonic approach towards the vertex, or in some instances, the stress-state rotates toward a vertex and then away.

2.7 Crystal plasticity modeling

The Micromechanical Analysis of Stress-Strain Inhomogeneities with fast Fourier transform (MASSIF) code (Lebensohn et al., 2012; Tari et al., 2018) was used to model the constitutive response of this alloy in the β solution heat treated and water quenched condition. The details of the model including the initial 3D microstructure instantiation and the model predictions are given elsewhere (Bhattacharyya et al., 2021). In this work, the results pertaining to the simulations carried out using the <111>{110} mode are considered. For comparison, the coaxiality with macroscopic stress and the stress misorientation were calculated according to the procedure described above, using the simulated grain-level stress values.

3. Results

The constitutive response obtained from the in-situ HEDM experiment is shown in Fig 2a. The numbered points denote different stages throughout the elastoplastic transition. The 3D near field reconstructed microstructure and relationship to the macroscopic sample are presented in Figure 2b.

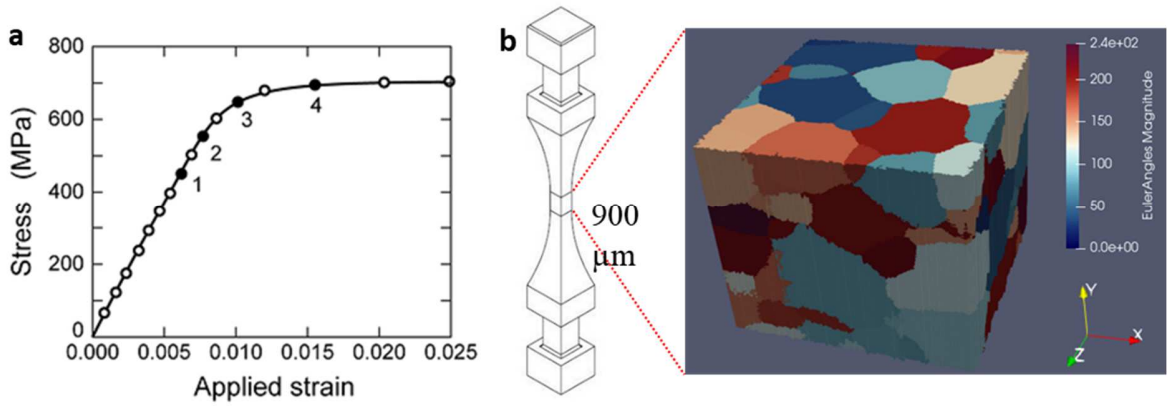

Figure 2 a) Stress strain curve obtained from the Timetal 18 specimen from the in-situ experiment. The black numbered points denote different stages throughout the elastoplastic transition: starting from elastic (1), microyielding (2 and 3) and fully plastic (4). **b)** The tensile specimen employed in this study, highlighting the gage section and the 3D reconstructed microstructure as obtained from the near-field experiment. The orientation map of the microstructure in the gage section, shows an essentially random initial texture of the material and that a significant fraction of the grains lies on the free surfaces.

To visualize the orientation of the stress tensor of a grain with respect to the polycrystalline specimen, it is convenient to use the stereographic projection and to map the eigenvectors (directions) of the stress tensor onto the unit sphere. Fig. 3a-c shows this schematically. The eigenvectors of the stress tensor of a grain is represented by the colored arrows with respect to the sample coordinates **x**, **y**, and **z**, where **y** is the macroscopic uniaxial loading direction. In the unloaded condition, the maximum principal stress (denoted by the red arrow) points in arbitrary directions which may be due to residual stress (Pokharel and Lebensohn, 2017; Tari et al., 2018). At the end of elastic loading, the maximum principal stress aligns closely with the macroscopic loading direction (Fig. 3b) and it remains aligned until the end of straining (Fig. 3c).

The direction of the maximum principal stress within several grains is projected onto the equatorial plane in Fig. 3d, under no load, at the end of elastic loading, and at an applied strain of 0.025. Fig. 3e shows the evolution of the angle between the eigenvector of the maximum

principal stress and the macroscopic loading direction, also known as coaxiality, with straining. As soon as the specimen is loaded, the stresses within the grains rapidly align with the loading direction and become increasingly coaxial as straining progresses. However, the average coaxiality changes very little (<2°) beyond a small, elastic strain level of ~ 0.3%. The fact that the stresses never align exactly with the macroscopic loading direction is a consequence of the elastic and plastic anisotropy of the material.

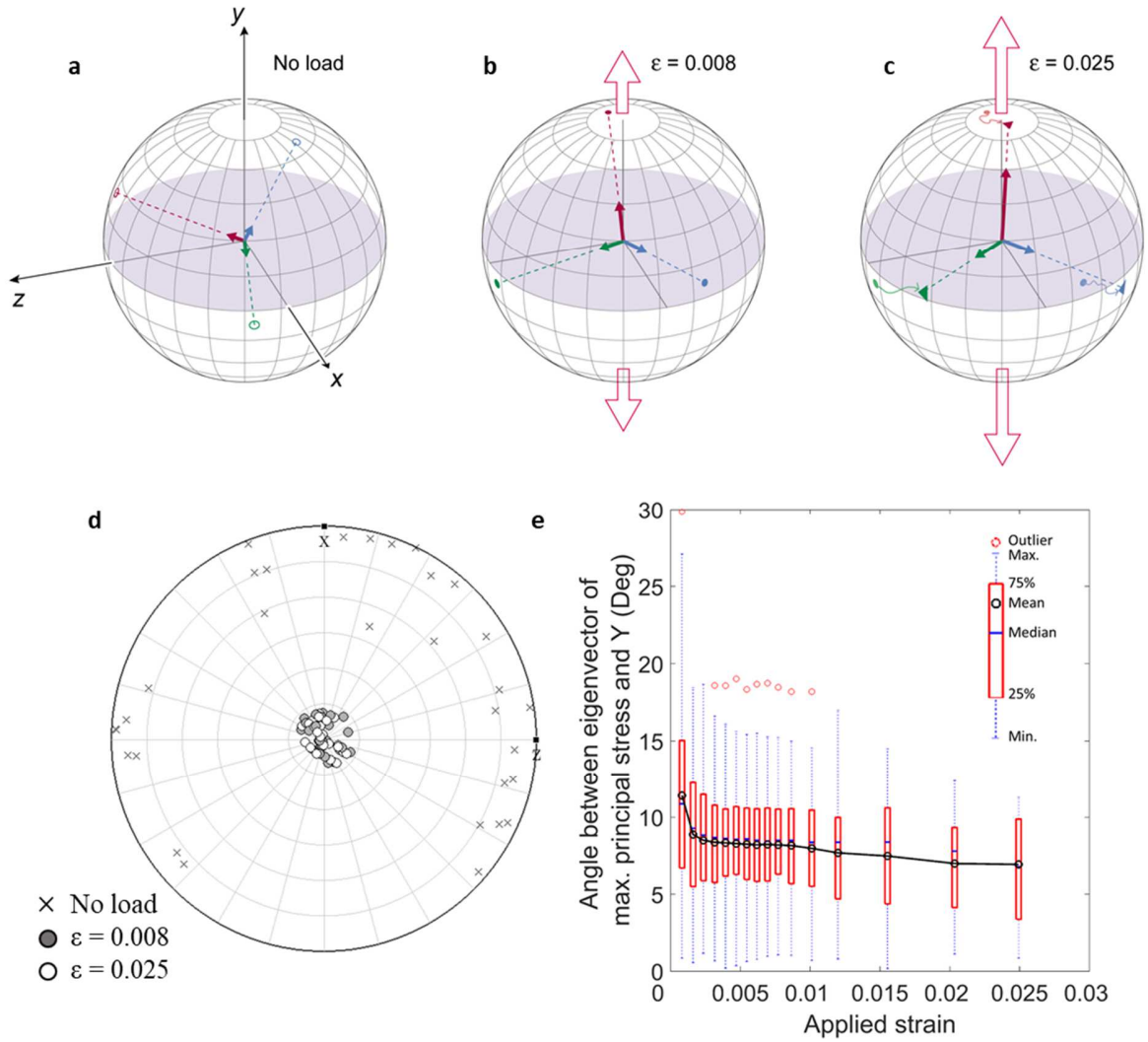

Figure 3. Unit sphere showing schematically the relationship between the eigenvectors (colored arrows) of the stress tensor of a grain and the sample coordinate system, **x, y,** and **z**, where **y** is the macroscopic loading direction, illustrating how the stress-state rotates with applied strain. **a**) In the unloaded condition, the maximum principal stress (red arrow) points in an arbitrary direction. **b**) At strain of 0.008, the maximum principal stress aligns closely with the macroscopic loading direction and **c**) It remains so until the end of straining, while the grain stress-state mainly rotates about the applied stress axis. **d)** Stereographic projection of the eigenvector of the largest principle stress showing that the stresses do align near the macroscopic loading axis at the center of the stereogram (**y**) in all the grains, but **e)** shows there is little change in the level of coaxiality from the proportional limit (strain of 0.008) and the final strain (0.025).

The evolution of the stress misorientation angle is shown as a function of applied strain in Fig. 4a. While the maximum principal stress component rotates by <2° during yielding (see Fig. 3e), the complete stress-state rotates, on average, by ~15° (see Fig. 4a), *providing the first direct experimental evidence of what was theoretically described by Kocks over 50 years ago* (1970). The stress misorientation rapidly evolves during the elastoplastic transition (yielding) and then plateaus once all the grains yield. Note also that these rotations are very large relative to the lattice reorientation of ~ 0.9°, on average (Fig. 4b). Such small lattice rotations are expected since the plastic strain imparted during the experiments is small, ~1.5%. The stress reorientation in some representative grains (Fig. 4c) show a rapid increase with strain throughout elastoplastic transition. These grains individually show a variety of constitutive responses including: a high strain hardening rate, near perfect plasticity, and even strain softening. The eigenvectors corresponding to all three principal stresses at successive strain levels are shown in stereographic projections, presented with respect to the sample coordinates (Fig. 4d). Examples from other grains are shown in Fig. 5. Note that in all cases, the rotation *towards* the loading direction only contributes a small portion to the total misorientation, while the major contributor is the rotation *about* the loading axis.

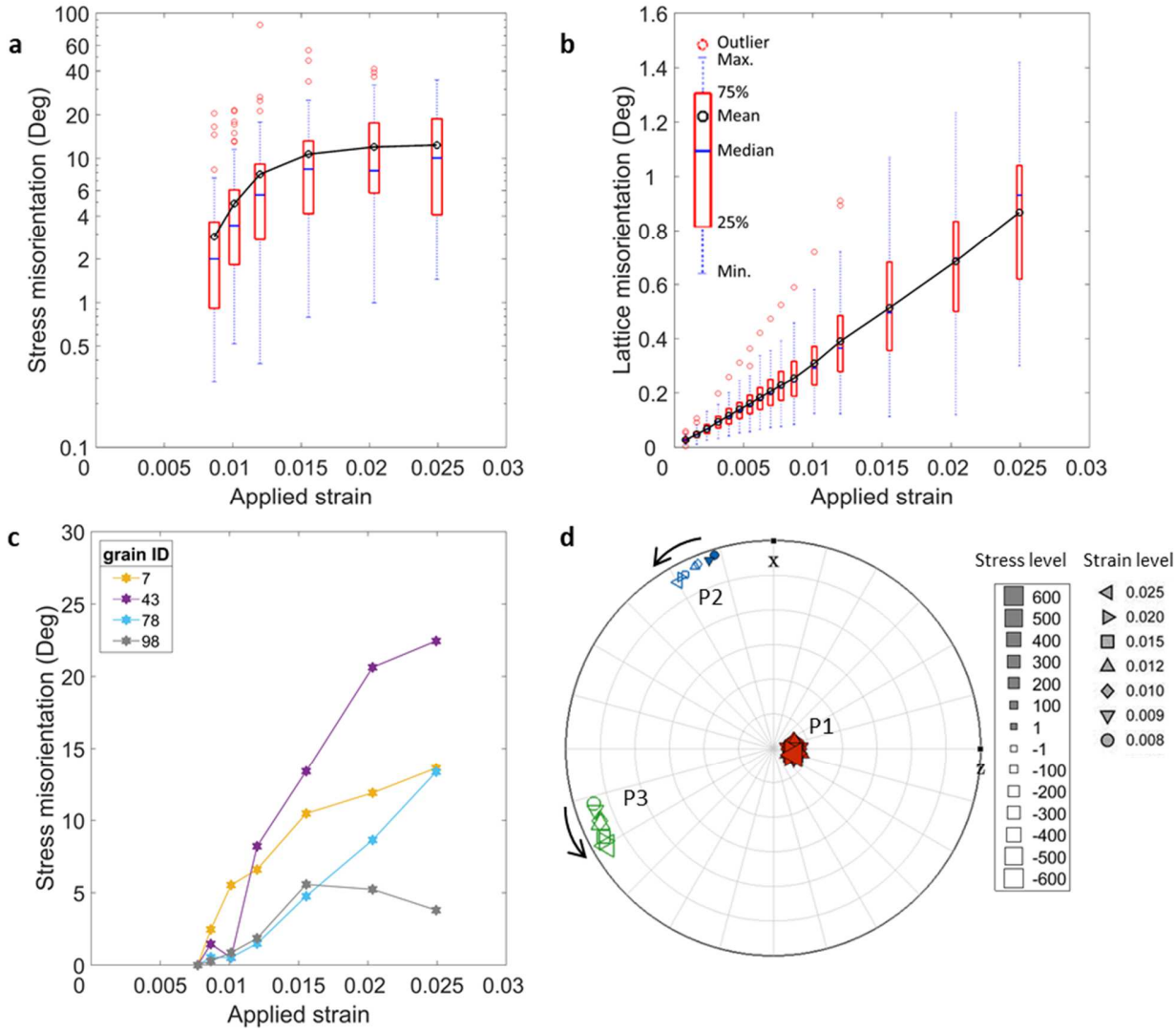

Figure 4. a) The stress state within the typical grain rotates an average of 15°. **b**) The evolution of lattice (crystallographic) orientation as a function of applied strain showing that the crystals only reorient on average, by 0.9°. **c**) The stress reorientation in representative grains throughout the elastoplastic transition, **d**) An example from a typical grain showing that the principal stress eigenvectors primarily rotate *about* the main loading axis, not *toward* it. The black arrows show the nature of the stress reorientation. P1 is the maximum and P3 is the minimum principal stress.

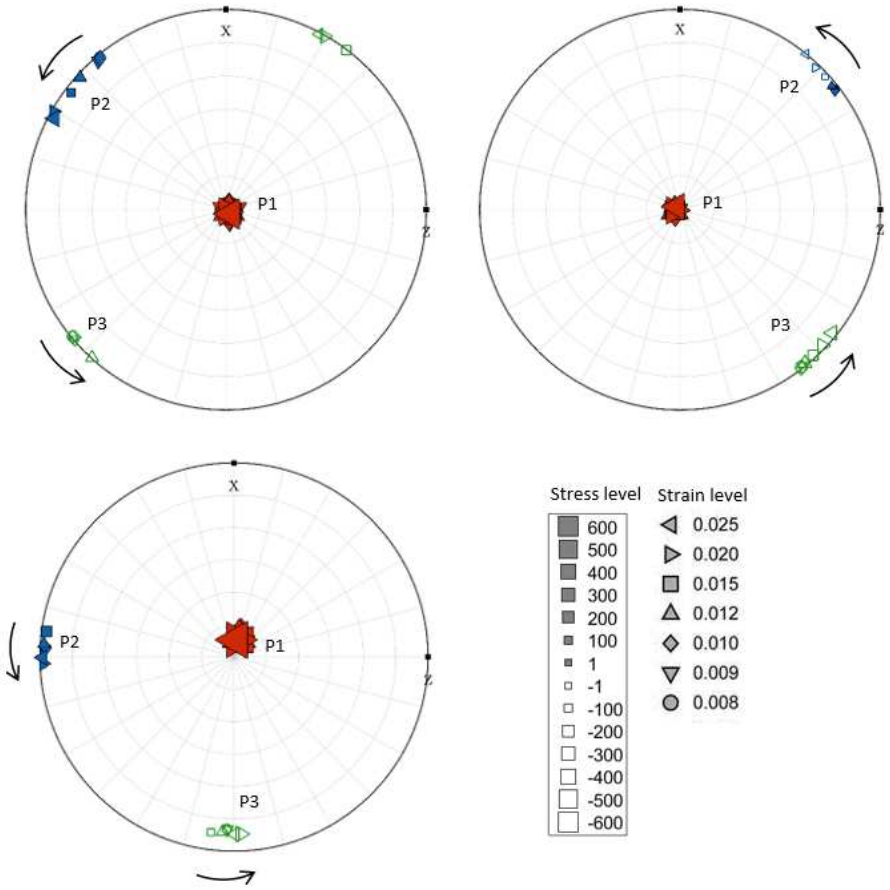

Figure 5. Examples of the stress reorientation in three representative grains showing that for all cases, this reorientation is primarily about the loading axis. The black arrows show the nature of the stress reorientation. P1 is the maximum and P3 is the minimum principal stress.

The stress-states of the grains are revealed to rotate about 5° (on average) *toward* the "target <111>{110} vertex" which is closest at the end of the elastoplastic transition (Fig. 6a). Examples from selected grains are shown in Fig. 6b. The coaxiality can either show a monotonic decrease in the angle between the stress-state and the vertex which is closest at an applied strain of 0.015, typically, after plasticity has commenced, or rotation away from the vertex, probably due to activation of another slip system, potentially one of the <111>{112} type slip systems. Additional crystal plasticity simulations suggest a change in slip mode and an associated change

in the direction of lattice rotation at the same point in straining (Bhattacharyya et al., 2021). Whereas an associated change in the direction of lattice reorientation could not be confidently detected experimentally, the change in the direction of stress rotation is readily detected. If one considers the coaxiality with the macroscopic (uniaxial) loading condition (see Fig. 3e), one finds that it reaches a limiting value early in the test (prior to yielding) and it does not further evolve. Thus, the results emphasize what has been stated on the basis of simulations; the grain-level stress state tends to rotate more toward the vertices in the SCYS than toward the macroscopic boundary conditions (Ritz et al., 2010).

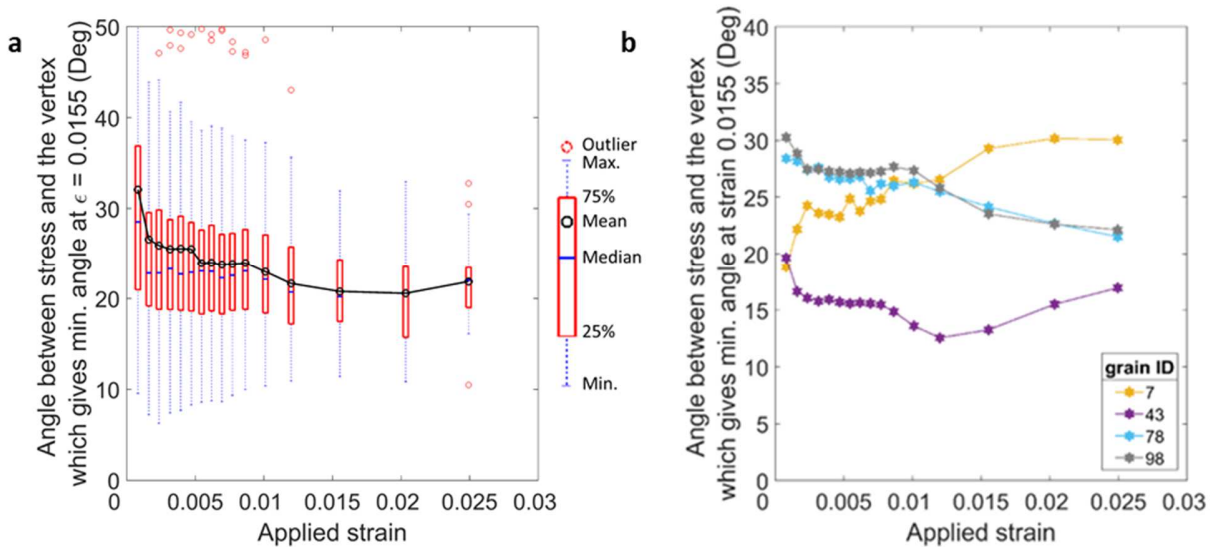

Figure 6. a) The stress-state of the grains rotate ~ 5°, on average, toward the "target vertex" during the elastoplastic transition, though they saturate at orientations which are still far from the vertices (~20°). **b)** The evolution of coaxiality with a vertex in representative grains showing either a monotonic decrease in the angle between the stress-state and the vertex which is closest at an applied strain of 0.015, typically, after plasticity has commenced, or rotation away from the vertex, probably due to activation of another slip system, potentially one of the <111>{112} type slip systems.

The results obtained from the MASSIF simulations are shown in Figs. 7 and 8. For the evolution of the angle between the eigenvector of the maximum principal stress and the macroscopic loading direction, (Fig. 7a), the MASSIF simulations also predict that the maximum stresses within the grains quickly align with the loading direction. After this initial, rapid alignment, the subsequent change in the average coaxiality is ~2°, in agreement with the experiment. Even in the simulations, the stresses never align exactly with the macroscopic loading direction thus confirming that this observation is due to the elastic and plastic anisotropy of the material. The MASSIF-predicted evolution of the stress misorientation angle is shown as a function of applied strain in Fig. 7b, and the complete stress-state rotates, on average, by ~15° which is very similar to that observed experimentally (see Fig. 4a). Although there are subtle differences in the experimental and simulated distributions at each strain level, the simulated results essentially show the same trend where the stress misorientation rapidly evolves during the elastoplastic transition and then tends to stall once all the grains yield. Even the variation among the grain populations is similar. However, on a grain-by-grain basis, the simulations do not match the experiment for every case (Fig. 7c), thought the agreement is satisfactory for some. Finally, the evolution of all the three predicted eigenvectors for the representative grains (Fig. 8) confirm that the major rotation of the stresses is indeed *about* the loading axis and not *towards* it. These simulation results further suggest that the major experimental observations presented in this paper are not due to experimental uncertainties.

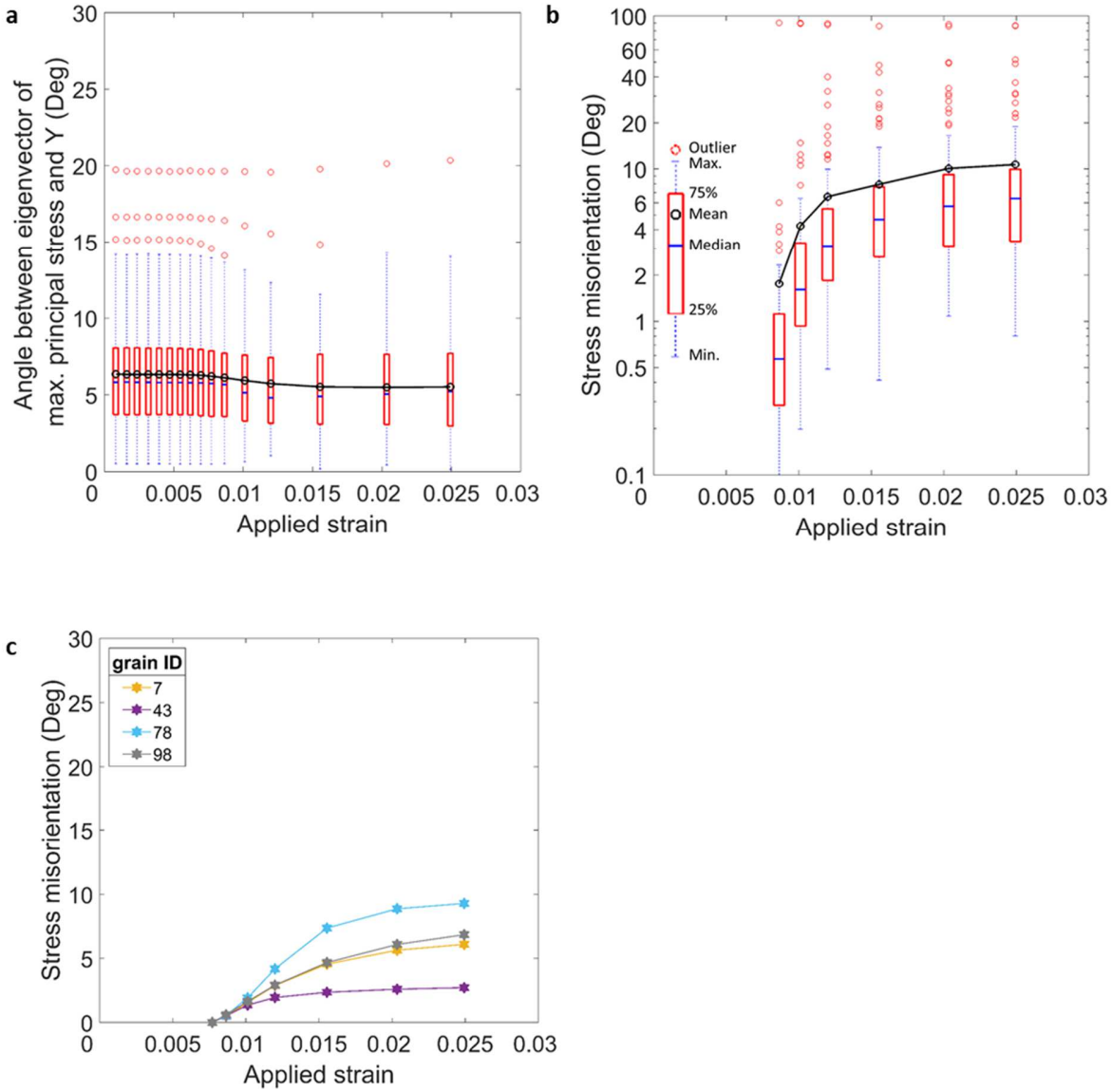

Figure 7. Results of MASSIF simulations **a)** showing that the coaxiality slightly decreases during yielding after which it stays essentially constant. **b)** The stress-state within the grains rotate on average by 15°, where the stress misorientation rapidly evolving during the elastoplastic transition and then tends to slow down once all the grains yield **c**) The stress reorientation in representative grains throughout the elastoplastic transition showing that the simulations predict a slightly lower (as compared to the experiment) stress reorientation for some grains while for others, the agreement is quite satisfactory.

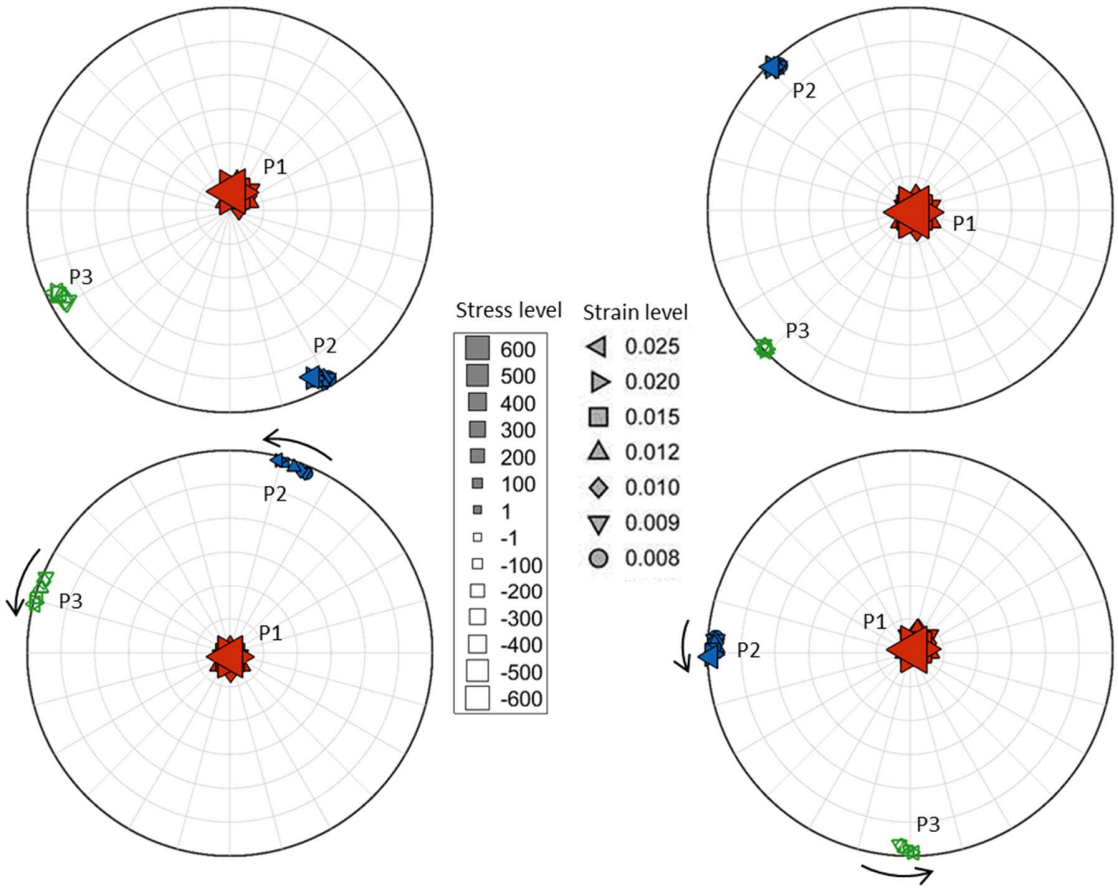

Figure 8. MASSIF simulations results of stress reorientation in the representative grains shown in Fig. 7c, showing that for all cases, this reorientation is primarily about the loading axis. The black arrows show the nature of the stress reorientation. P1 is the maximum and P3 is the minimum principal stress.

4. Discussion

The experimental results highlight that the rotations of the stress-state predicted by theory are observable. Furthermore, they are large, relative to the rigid body and lattice rotations which crystals undergo during the elastoplastic transition. Furthermore, although the stresses tend to rotate toward a vertex, the rotations saturate by the end of the elastoplastic transition, and the stress-states are still far from the vertices (~20°). This is expected because of the following reasons:

1. Most metals and alloys are rate insensitive at ambient temperatures, but not entirely rate independent. Hence, there is a finite curvature at a vertex in a real SCYP, (Fig. 1), and the stress-state need not get into a vertex to activate multiple slip systems, only get close to it.
2. Dislocations within BCC metals may glide on multiple types of slip planes, {110}, {112}, {123}, etc. (Castany et al., 2012; Wang et al., 2020). Kocks (1970) highlighted that under such conditions, the stress-state in the grains do not have to go to a vertex, rather "edges" of the SCYS are sufficient. Kocks (1970) further pointed out that all of the vertices involving 5 or more slip systems are occluded (outside the SCYS). Later studies (Piehler and Backofen, 1971; Raphanel and Schmitt, 1984; Schmitt and Raphanel, 1986) confirmed that combinations of 3 or 4 such "pencil glide" slip systems are sufficient to accommodate any general strain. Again, we provide some of the first experimental evidence of a theory which was essentially laid out 50 years ago, but the experimental proofs have been lacking ever since.
3. It has been previously noted that interactions between many slip systems result in high energy dislocation configurations (Bay et al., 1992). This is why grains break into subdomains, within which only 1-3 slip systems operate (Gioacchino and da Fonseca, 2015). The specific slip systems which are active vary from one subdomain to another, and this allows the entire grain to maintain compatibility and low stored energy.
4. The microstructure of the interrogated gage volume (see Fig. 2b) reveals that a large fraction of the grains is exposed to the free surface of the sample, i.e. they are not completely surrounded (have at least one free surface) and, therefore, are not as constrained as typical grains within a bulk polycrystal. Fewer active slip systems can accommodate plasticity in such cases, and therefore, the stress-state is not required to reach a vertex.

Our results demonstrate that the alignment of the stresses with the macroscopic loading direction is only a small part of the stress reorientation, though it had been the focus of prior investigations (Lienert et al., 2009; Chatterjee et al., 2016; Juul et al., 2017; Turner et al., 2017). Actually, the grain stress states mainly rotate *about* the applied stress axis and *not toward* it (see Figs. 3e, 4d, and 5). It is mainly the stress components which are normal to the applied stress axis which change significantly. Hence, the eigenvectors corresponding to these principle stresses as well as the eigenvalues change the most. To illustrate an observed connection between these changes in the eigenvalues and spatial location, the stress triaxiality is plotted as a function of the distance of the grain centroid position from the center, on the **x**-**z** plane in Fig. 9a. The grains near the surface tend to have a lower triaxiality, though the correlation is weak. This is not surprising, because the lack of constraint on surface grains permits them to plastically relax. However, it can have significant consequences under fatigue loading, in particular, since it is known that persistent slip band formation in surface grains can lead to crack nucleation via an intrusion/extrusion mechanism (Mughrabi, 2009; Sangid, 2013; Polák and Man, 2014; Polák et al., 2017; Lavenstein et al., 2020). Obviously, the grains in the interior would be forced to have a higher triaxiality in order to ensure that the volume averaged stress state of the grains is equivalent to the macroscopically enforced uniaxial tensile loading condition. Admittedly, this spatial variation in triaxiality would be less be less obvious in a polycrystal with more grains in the cross-section, but the surface effects would still be present.

Also note that the stress triaxiality strongly correlates with the values of the intermediate and the lowest principal stress values (Fig. 9b and c). The grains that strain soften (red symbols) tend to have a low stress triaxiality associated with $\sigma_2 \approx 0$ and σ_3 is large in magnitude and negative (compressive). On the other hand, the grains that undergo strong strain hardening (black

symbols) tend to have higher triaxiality, a positive σ_2, and $\sigma_3 \approx 0$. Notably, these hardening grains tend towards a stress-state of plane strain tension. Further compelling evidence is provided in Fig. 9d, where data show that the median change in triaxiality is zero for the hardening grains, and the mean value is slightly positive, which implies that the triaxiality of these grains tend to remain unchanged or slightly increase during plasticity. On the other hand, the majority (>75%) of the softening grains have decreasing triaxiality in the plastic regime.

Figure 9e shows a slice through a tomogram obtained after failure had initiated within the monotonically loaded specimen. Fracture has clearly originated at the center of the specimen where damage (e.g. microvoids) nucleates in grains with high triaxiality. However, subsequent growth and coalescence of this damage is mediated by shear localization toward the surface (Noell et al., 2018; Pineau et al., 2016). The present study highlights two different types of "hot spots" vis a vis failure – high triaxiality (microvoid nucleation, growth and coalescence) and low triaxiality – shear, recently highlighted as important in some monotonic failures (Bao and Wierzbicki, 2004; Bao, 2005; Nahshon and Hutchinson, 2008; Tekoğlu et al., 2015), but also a potential issue for fatigue failure (Sangid, 2013).

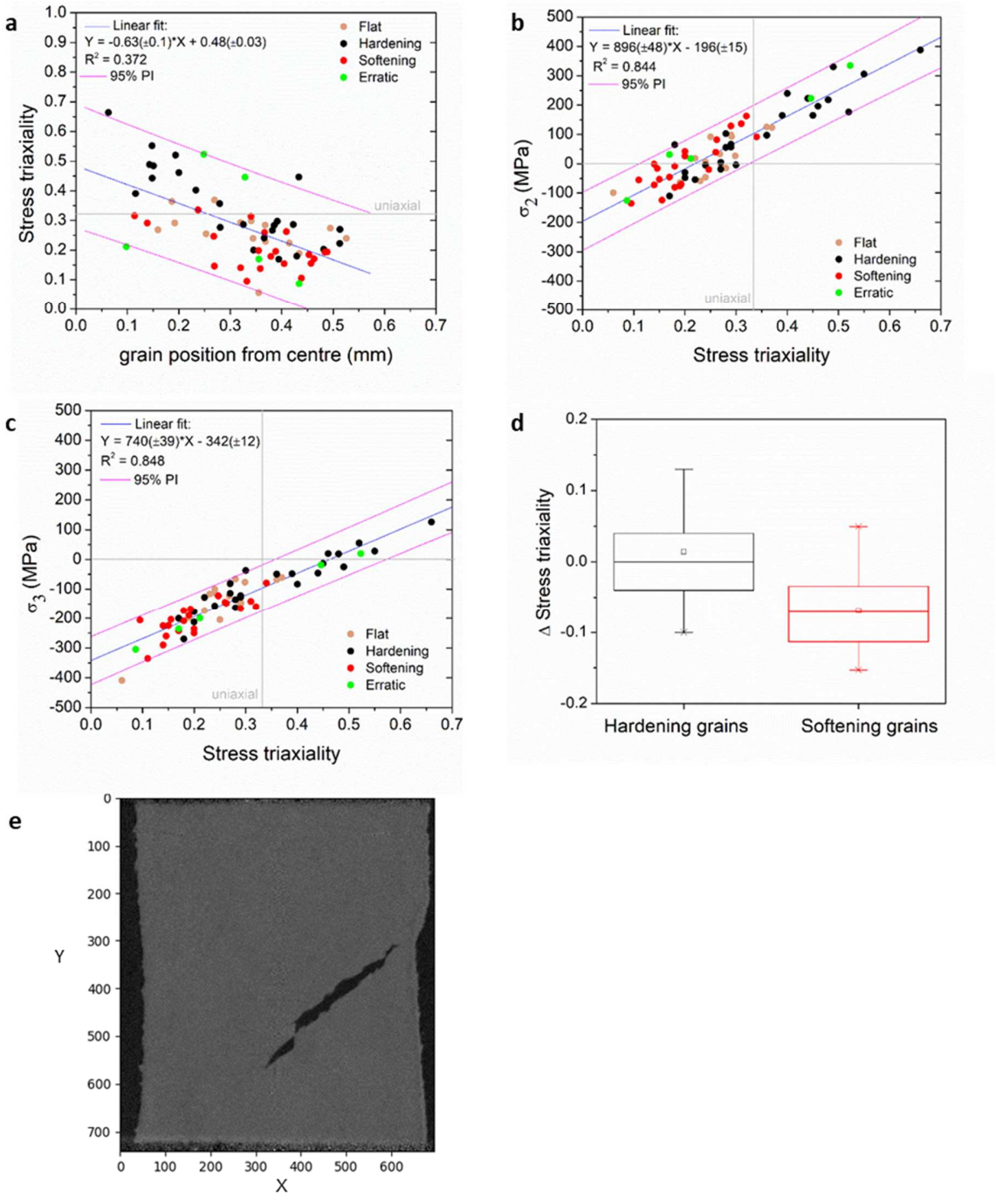

Figure 9. a) The grains closer to the free surface tends to have low triaxiality. The relationship between stress triaxiality with **b)** the intermediate principal stress and **c)** the minimum principal stress, showing that the grains that undergo strain softening (red symbols in the figure) tend to have a low stress triaxiality, whereas the grains that undergo strong strain hardening tend to have higher triaxiality values and tend towards a stress-state of plane strain tension. **d)** The change in

stress triaxiality for grains that undergo strain hardening and strain softening, showing that the median change in triaxiality is zero and the mean value is slightly positive in grains which harden. On the other hand, the majority (>75%) of the softening grains have lowered their triaxiality in the plastic regime. **e)** A 2D slice through a tomogram obtained after failure has initiated showing that fracture has occurred via shear localization.

Finally, it is reiterated that the essential trends observed experimentally are well-captured by the MASSIF simulations, whereas there are still a few discrepancies at the individual grain level. (Compare results of Figs. 7 & 8 with those of 4 & 5.) A similar conclusion was reached previously where it was shown that the overall constitutive response could be modelled quite accurately, yet there remain significant discrepancies at the individual grain level (Bhattacharyya et al., 2021). Note, this is also true for other fields in materials science, such as grain growth, where it was recently noted that, while grain growth models successfully capture the kinetics of grain growth at the aggregate level, there can be severe discrepancies in grain boundary mobility values as obtained from synchrotron based in-situ grain growth experiment (Zhang et al., 2020). Thus, these new in-situ 3D characterization techniques enable direct comparison between experiments and offers an entirely new avenue to validate existing models in an unprecedented way.

5. Concluding Remarks

The results from MASSIF full-field crystal plasticity simulations clearly show that the stress rotations presented in this paper is not a result of experimental errors or uncertainties. It is thus possible that combining knowledge of such stress rotations with statistical descriptions of microstructure could reveal previously unrealized vulnerabilities in materials. New techniques of nondestructive evaluation could be developed to help avoid premature failures. Alternatively,

microstructures could be designed for particular loading conditions to have attributes which would avoid such stress conditions. Indeed, this would take microstructure design beyond the simple ones which materials scientists have employed to date... focusing on grain and particle size and shape, and even texture (1-point statistics). The present insight demands at least 2-point statistics (Fullwood et al., 2010; Paulson et al., 2017), e.g. correlations between the orientations of crystals and their spatial relationships, since neighboring grains have such a strong impact upon the stress state of an individual grain. Indeed, this also provides a new framework for researchers to interpret the observation that grain neighborhood can be as important as grain orientation itself (Sarma and Dawson, 1996). It highlights why 2-site and cluster-type models have proven useful for predicting materials responses such as texture evolution during large strain materials processing (Engler et al., 2005; Van Houtte et al., 2005; Mu et al., 2011, 2014).

Acknowledgments

We thank Prof. Haitham El-Kadiri and Dr. Andrew Oppedal (Mississippi State University) and the Army Research Laboratory (ARL) for providing us with the Timetal-18 samples.

Funding: The research at University of Virginia was sponsored by the US Department of Energy, Basic Energy Sciences, Mechanical Behavior and Radiation Effects Program led by Dr. John Vetrano, Grant # DE-SC0018923. The data for this paper was collected at the Center for High Energy X-ray Sciences (CHEXS) which is supported by the National Science Foundation under award DMR-1829070.

Data and materials availability: The raw data is available as diffraction patterns which are stored at the CHESS repository.

References

Bao, Y., 2005. Dependence of ductile crack formation in tensile tests on stress triaxiality, stress and strain ratios. Eng. Fract. Mech. 72, 505–522. https://doi.org/10.1016/j.engfracmech.2004.04.012

Bao, Y., Wierzbicki, T., 2004. On fracture locus in the equivalent strain and stress triaxiality space. Int. J. Mech. Sci. 46, 81–98. https://doi.org/10.1016/j.ijmecsci.2004.02.006

Bay, B., Hansen, N., Hughes, D.A., Kuhlmann-Wilsdorf, D., 1992. Overview no. 96 evolution of f.c.c. deformation structures in polyslip. Acta Metall. Mater. 40, 205–219. https://doi.org/10.1016/0956-7151(92)90296-Q

Becker, R., Panchanadeeswaran, S., 1989. Crystal Rotations Represented as Rodrigues Vectors. Textures Microstruct. 10, 167–194. https://doi.org/10.1155/tsm.10.167

Bernier, J. V, Barton, N.R., Lienert, U., Miller, M.P., 2011. Far-field high-energy diffraction microscopy : a tool for intergranular orientation and strain analysis. J. Strain Anal. 46, 527–547. https://doi.org/10.1177/0309324711405761

Bhattacharyya, J.J., Nair, S., Pagan, D.C., Tari, V., Lebensohn, A., Rollett, A.D., Agnew, S.R., 2021. Elastoplastic transition in a metastable β -Titanium alloy , Timetal-18 – An in-situ synchrotron X-ray diffraction study. Int. J. Plast. 139, 102947. https://doi.org/10.1016/j.ijplas.2021.102947

Bhattacharyya, J.J., Nair, S., Rollett, A., Pagan, D.C., Tari, V., Agnew, S.R., 2020. In-situ high energy X-ray diffraction study of the elastic response of a metastable β-titanium alloy. Acta Mater. 197, 300–308.

Blank, B.E., Schuren, J., Shade, P., Turner, T., 2016. Rotational and axial motion system and methods of use.

Castany, P., Besse, M., Gloriant, T., 2012. In situ TEM study of dislocation slip in a metastable β titanium alloy. Scr. Mater. 66, 371–373. https://doi.org/10.1016/j.scriptamat.2011.11.036

Chatterjee, K., Venkataraman, A., Garbaciak, T., Rotella, J., Sangid, M.D., Beaudoin, A.J., Kenesei, P., Park, J.S., Pilchak, A.L., 2016. Study of grain-level deformation and residual stresses in Ti-7Al under combined bending and tension using high energy diffraction microscopy (HEDM). Int. J. Solids Struct. 94–95, 35–49. https://doi.org/10.1016/j.ijsolstr.2016.05.010

Edmiston, J.K., Barton, N.R., Bernier, J. V, Johnson, C., Steigmann, D.J., 2011. Precision of lattice strain and orientation measurements using high-energy monochromatic X-ray diffraction 299–312. https://doi.org/10.1107/S0021889811002123

Edmiston, J.K., Bernier, J. V, Barton, R., Johnson, G.C., 2012. Lattice refinement strategies 181–187. https://doi.org/10.1107/S010876731105598X

Engler, O., Crumbach, M., Li, S., 2005. Alloy-dependent rolling texture simulation of aluminium alloys with a grain-interaction model. Acta Mater. 53, 2241–2257. https://doi.org/10.1016/j.actamat.2005.01.032

Fanning, J., 2011. Properties of TIMETAL 18 - A New High-Strength Titanium Forging Alloy, in: The 22nd Advanced Aerospace Materials and Processes (AeroMat) Conference and Exposition of ASM.

Fullwood, D.T., Niezgoda, S.R., Adams, B.L., Kalidindi, S.R., 2010. Microstructure sensitive design for performance optimization. Prog. Mater. Sci. 55, 477–562.

https://doi.org/10.1016/j.pmatsci.2009.08.002
Gagg, C.R., Lewis, P.R., 2009. In-service fatigue failure of engineered products and structures - Case study review. Eng. Fail. Anal. 16, 1775–1793. https://doi.org/10.1016/j.engfailanal.2008.08.008
Gioacchino, F. Di, da Fonseca, J.Q., 2015. An experimental study of the polycrystalline plasticity of austenitic stainless steel. Int. J. Plast. 74, 92–109. https://doi.org/10.1016/j.ijplas.2015.05.012
Gürsoy, D., De Carlo, F., Xiao, X., Jacobsen, C., 2014. TomoPy: A framework for the analysis of synchrotron tomographic data. J. Synchrotron Radiat. 21, 1188–1193. https://doi.org/10.1107/S1600577514013939
Han, T.S., Chung, S.Y., 2012. Dependence of crystal stress evolution on the vertices of the single crystal yield surface and the effect from the intergranular misorientation during plastic deformation. Comput. Mater. Sci. 63, 35–46. https://doi.org/10.1016/j.commatsci.2012.05.064
Han, T.S., Chung, S.Y., Cho, J.H., 2012. Investigation of crystal stress dependence on lattice orientation, loading direction, and grain interactions in a plastically deforming crystal embedded within a polycrystal aggregate. Mater. Sci. Eng. A 552, 252–268. https://doi.org/10.1016/j.msea.2012.05.038
Han, T.S., Chung, S.Y., Lee, B., 2013. Crystal stress distribution evolution of elastoplastically deforming polycrystals over crystal orientation space. Comput. Mater. Sci. 75, 9–17. https://doi.org/10.1016/j.commatsci.2013.03.031
Jakobsen, B., Poulsen, H.F., Lienert, U., Almer, J., Shastri, S.D., Sørensen, H.O., Gundlach, C., Pantleon, W., 2006. Formation and subdivision of deformation structures during plastic deformation. Science (80-.). 312, 889–892. https://doi.org/10.1126/science.1124141
Jakobsen, B., Poulsen, H.F., Lienert, U., Pantleon, W., 2007. Direct determination of elastic strains and dislocation densities in individual subgrains in deformation structures. Acta Mater. 55, 3421–3430. https://doi.org/10.1016/j.actamat.2007.01.049
Juul, N.Y., Oddershede, J., Beaudoin, A., Chatterjee, K., Koker, M.K.A., Dale, D., Shade, P., Winther, G., 2017. Measured resolved shear stresses and Bishop-Hill stress states in individual grains of austenitic stainless steel. Acta Mater. 141, 388–404. https://doi.org/10.1016/j.actamat.2017.09.021
Kocks, U.F., 1970. The relation between polycrystal deformation and single-crystal deformation. Metall. Mater. Trans. 1, 1121–1143. https://doi.org/10.1007/BF02900224
Kocks, U.F., Canova, G.R., Jonas, J.J., 1983. Yield vectors in f.c.c. crystals. Acta Metall. 31, 1243–1252. https://doi.org/10.1016/0001-6160(83)90186-4
Lavenstein, S., Gu, Y., Madisetti, D., El-Awady, J.A., 2020. The heterogeneity of persistent slip band nucleation and evolution in metals at the micrometer scale. Science (80-.). 370. https://doi.org/10.1126/science.abb2690
Lebensohn, R.A., Kanjarla, A.K., Eisenlohr, P., 2012. An elasto-viscoplastic formulation based on fast Fourier transforms for the prediction of micromechanical fields in polycrystalline materials. Int. J. Plast. 32–33, 59–69. https://doi.org/10.1016/j.ijplas.2011.12.005
Lebrun, E., Svec, P., Nowak, S., Denand, B., Millet, Y., Prima, F., 2014. Phase Transformations of TIMETAL-18 as a New Titanium Alloy with Bimodal Microstructure, in: Advanced Materials Research. pp. 418–423.
Lee, E.H., Stoughton, T.B., Yoon, J.W., 2018. Kinematic hardening model considering

directional hardening response. Int. J. Plast. 110, 145–165. https://doi.org/10.1016/j.ijplas.2018.06.013
Lee, E.H., Stoughton, T.B., Yoon, J.W., 2017. A yield criterion through coupling of quadratic and non-quadratic functions for anisotropic hardening with non-associated flow rule. Int. J. Plast. 99, 120–143. https://doi.org/10.1016/j.ijplas.2017.08.007
Lienert, U., Brandes, M.C., Bernier, J. V., Weiss, J., Shastri, S.D., Mills, M.J., Miller, M.P., 2009. In situ single-grain peak profile measurements on Ti-7Al during tensile deformation. Mater. Sci. Eng. A 524, 46–54. https://doi.org/10.1016/j.msea.2009.06.047
Lou, Y., Yoon, J.W., Huh, H., 2014. Modeling of shear ductile fracture considering a changeable cut-off value for stress triaxiality. Int. J. Plast. 54, 56–80. https://doi.org/10.1016/j.ijplas.2013.08.006
Mu, S., Al-Samman, T., Mohles, V., Gottstein, G., 2011. Cluster type grain interaction model including twinning for texture prediction: Application to magnesium alloys. Acta Mater. 59, 6938–6948. https://doi.org/10.1016/j.actamat.2011.07.045
Mu, S., Tang, F., Gottstein, G., 2014. A cluster-type grain interaction deformation texture model accounting for twinning-induced texture and strain-hardening evolution: Application to magnesium alloys. Acta Mater. 68, 310–324. https://doi.org/10.1016/j.actamat.2013.12.007
Mughrabi, H., 2009. Cyclic slip irreversibilities and the evolution of fatigue damage. Metall. Mater. Trans. B Process Metall. Mater. Process. Sci. 40, 431–453. https://doi.org/10.1007/s11663-009-9240-4
Nahshon, K., Hutchinson, J.W., 2008. Modification of the Gurson Model for shear failure. Eur. J. Mech. A/Solids 27, 1–17. https://doi.org/10.1016/j.euromechsol.2007.08.002
Noell, P.J., Carroll, J.D., Boyce, B.L., 2018. The mechanisms of ductile rupture. Acta Mater. 161, 83–98. https://doi.org/10.1016/j.actamat.2018.09.006
Papasidero, J., Doquet, V., Mohr, D., 2015. Ductile fracture of aluminum 2024-T351 under proportional and non-proportional multi-axial loading: Bao-Wierzbicki results revisited. Int. J. Solids Struct. 69–70, 459–474. https://doi.org/10.1016/j.ijsolstr.2015.05.006
Paulson, N.H., Priddy, M.W., McDowell, D.L., Kalidindi, S.R., 2017. Reduced-order structure-property linkages for polycrystalline microstructures based on 2-point statistics. Acta Mater. 129, 428–438. https://doi.org/10.1016/j.actamat.2017.03.009
Piehler, H.., Backofen, W.., 1971. A theoretical examination of the plastic properties of BCC crystals deforming by <111> pencil glide. Metall. Trans. 2, 249–255.
Pineau, A., Benzerga, A.A., Pardoen, T., 2016. Failure of metals I: Brittle and ductile fracture. Acta Mater. 107, 424–483. https://doi.org/10.1016/j.actamat.2015.12.034
Pokharel, R., Lebensohn, R.A., 2017. Instantiation of crystal plasticity simulations for micromechanical modelling with direct input from microstructural data collected at light sources. Scr. Mater. 132, 73–77. https://doi.org/10.1016/j.scriptamat.2017.01.025
Polák, J., Man, J., 2014. Mechanisms of extrusion and intrusion formation in fatigued crystalline materials. Mater. Sci. Eng. A 596, 15–24. https://doi.org/10.1016/j.msea.2013.12.005
Polák, J., Mazánová, V., Heczko, M., Petráš, R., Kuběna, I., Casalena, L., Man, J., 2017. The role of extrusions and intrusions in fatigue crack initiation. Eng. Fract. Mech. 185, 46–60. https://doi.org/10.1016/j.engfracmech.2017.03.006
Raphanel, J.., Schmitt, J.., 1984. A geometrical and physical description of yield surfaces for b.c.c. crystals in pencil glide. Mater. Sci. Eng. A 64, 255–263.
Ritz, H., Dawson, P., Marin, T., 2010. Analyzing the orientation dependence of stresses in

polycrystals using vertices of the single crystal yield surface and crystallographic fibers of orientation space. J. Mech. Phys. Solids 58, 54–72. https://doi.org/10.1016/j.jmps.2009.08.007
Sangid, M.D., 2020. Coupling in situ experiments and modeling – Opportunities for data fusion, machine learning, and discovery of emergent behavior. Curr. Opin. Solid State Mater. Sci. 24, 100797. https://doi.org/10.1016/j.cossms.2019.100797
Sangid, M.D., 2013. The physics of fatigue crack initiation. Int. J. Fatigue 57, 58–72. https://doi.org/10.1016/j.ijfatigue.2012.10.009
Sarma, G.B., Dawson, P.R., 1996. Effects of interactions among crystals on the inhomogeneous deformations of polycrystals. Acta Mater. 44, 1937–1953. https://doi.org/10.1016/1359-6454(95)00309-6
Schmitt, J.H., Raphanel, J.L., 1986. Yield surfaces of b.c.c. crystals with crystallographic slip. Mater. Sci. Eng. 80, 31–35. https://doi.org/10.1016/0025-5416(86)90209-0
Shade, P.A., Blank, B., Schuren, J.C., Turner, T.J., Kenesei, P., Goetze, K., Robert, M., Bernier, J. V, Li, S.F., Lind, J., Lienert, U., Almer, J., Shade, P.A., Blank, B., Schuren, J.C., Turner, T.J., Kenesei, P., Goetze, K., Suter, R.M., Bernier, J. V, Li, S.F., Lind, J., Lienert, U., Almer, J., 2015. A rotational and axial motion system load frame insert for in situ high energy x-ray studies energy x-ray studies. Rev. Sci. Instrum 86. https://doi.org/10.1063/1.4927855
Tari, V., Lebensohn, R.A., Pokharel, R., Turner, T.J., Shade, P.A., Bernier, J. V, Rollett, A.D., 2018. Validation of micro-mechanical FFT-based simulations using High Energy Diffraction Microscopy on Ti-7Al. Acta Mater. 154, 273–283. https://doi.org/10.1016/j.actamat.2018.05.036
Tekoğlu, C., Hutchinson, J.W., Pardoen, T., 2015. On localization and void coalescence as a precursor to ductile fracture. Philos. Trans. R. Soc. A Math. Phys. Eng. Sci. 373, 20140121.
Turner, T.J., Shade, P.A., Bernier, J. V., Li, S.F., Schuren, J.C., Kenesei, P., Suter, R.M., Almer, J., 2017. Crystal Plasticity Model Validation Using Combined High-Energy Diffraction Microscopy Data for a Ti-7Al Specimen. Metall. Mater. Trans. A Phys. Metall. Mater. Sci. 48, 627–647. https://doi.org/10.1007/s11661-016-3868-x
Van Houtte, P., Li, S., Seefeldt, M., Delannay, L., 2005. Deformation texture prediction: from the Taylor model to the advanced Lamel model, International Journal of Plasticity. https://doi.org/10.1016/j.ijplas.2004.04.011
Wang, F., Balbus, G.H., Xu, S., Su, Y., Shin, J., Rottmann, P.F., Knipling, K.E., Stinville, J.C., Mills, L.H., Senkov, O.N., Beyerlein, I.J., Pollock, T.M., Gianola, D.S., 2020. Multiplicity of dislocation pathways in a refractory multiprincipal element alloy. Science (80-.). 370, 95–101. https://doi.org/10.1126/science.aba3722
Zhang, J., Ludwig, W., Zhang, Y., Sørensen, H.H.B., Rowenhorst, D.J., Yamanaka, A., Voorhees, P.W., Poulsen, H.F., 2020. Grain boundary mobilities in polycrystals. Acta Mater. 191, 211–220. https://doi.org/10.1016/j.actamat.2020.03.044